Mathematical Biosciences and Engineering

MBE, 18 (6): 9381–9393.
DOI: 10.3934/mbe.2021461
Received: 20 July 2021
Accepted: 15 October 2021
Published: 28 October 2021

http://www.aimspress.com/journal/MBE

Research article

Modeling of external self-excitation and force generation on magnetic nanoparticles inside vitreous cavity

Evan Parker[1], Chandler S. Mitchell[2], Joshua P Smith[1], Evan Carr[2], Rasul Akbari[1], Afshin Izadian[1] and Amir R Hajrasouliha[2,*]

[1] School of Engineering and Technology, Indiana University Purdue University, Indianapolis, IN 46202, USA
[2] Eugene and Marilyn Glick Eye Institute, Department of Ophthalmology, Indiana University School of Medicine, Indianapolis, IN 46202, USA

* **Correspondence:** Email: amhjaras@iu.edu; Tel: +1-377-944-202.

Abstract: The purpose of this manuscript was to design a better method for recovery from rhegmatogenous retinal detachment (RRD) surgery. We attempted to achieve this by designing a helmet that can manipulate intraocular magnetic nanoparticles (MNPs) and create a magnetic tamponade, eliminating the need for postoperative head positioning. A simulated analysis was developed to predict the pattern of magnetic force applied to the magnetic nanoparticles by external magnetic field. No participants were involved in this study. Instead, magnetic flux and force data for three different helmet designs were collected using virtual simulation tools. A prototype helmet was then constructed and magnetic flux and force data were recorded and compared to virtual data. For both virtual and physical scenarios, magnitude and direction of the resulting forces were compared to determine which design created the controlled direction and strongest forces into the back of the eye. Of the three virtual designs, both designs containing a visor had greater force magnitude than magnet alone. Between both designs with visors, the visor with bends resulted in forces more directed at the back of the eye. The physical prototype helmet shared similar measurements to virtual simulation with minimal percent error (Average = 5.47%, Standard deviation = 0.03). Of the three designs, the visor with bends generated stronger forces directed at the back of the eye, which is most appropriate for creating a tamponade on the retina. We believe that this design has shown promising capability for manipulating intraocular MNPs for the purpose of creating a tamponade for RRD.

Keywords: magnetic; nanoparticle; helmet; retinal; detachment

Abbreviations: RRD: Rhegmatogenous retinal detachment; PPV: Pars Plana Vitrectomy; PR: Pneumatic retinopexy; MNP: Magnetic Nanoparticle

1. Introduction

Rhegmatogenous retinal detachment (RRD) occurs when vitreous fluid enters the subretinal space through a break within the retina. RRD is an ocular emergency that involves surgical reattachment to restore compromised visual function before the loss is irreversible. There are three primary techniques for reattachment: pars plana vitrectomy (PPV), pneumatic retinopexy (PR), or application of a scleral buckle [1]. PPV and PR techniques account for most surgical attachments, composing about 74% and 15% of retinal reattachments, respectively [2]. While at their core both procedures utilize cryopexy or laser photocoagulation to adhere the retina to the RPE, it is common for both procedures to involve the injection of an intraocular bubble (gas or in silicon oil) to assist with the reattachment [3]. With specific head positioning, the bubble acts as an endotamponade within the eye, preventing fluid from passing through the repair. Additionally, its buoyant and hydraulic forces press the retina into the RPE to further facilitate chorioretinal adhesion during the postoperative period while the subretinal fluid is absorbed [4].

There is strong data suggesting that the formation of adhesion with optimal tensile strength takes 7–14 days, and maintenance of a gas tamponade against the retinal break is considered essential to this process [5–9]. Depending on the location of the break, a specific head positioning is required throughout this recovery period. However, posturing of the head during this time span can be a major inconvenience for patients, especially for those with inferior tears that require prone or head-inferior positioning and in pediatric cases. Many surgeons therefore ask their patients to follow strict positioning recommendations for at least 3–7 days [10,11]. Still, posturing for even this shortened timespan is difficult and can be affected by physical constraints such as arthritis or body habitus. Additionally, prolonged positioning can cause compression sores, deep vein thrombosis, among other complications [4]. Consequently, many patients demonstrate poor compliance with positioning recommendations, and this been proven to be a culprit for failed procedures [12]. This dissonance between the importance of patient positioning compliance for successful reattachment and the reality that compliance is historically poor points to the need for an alternate method to obviate the need for long-term tamponade determined by patient positioning. The solution may lie with the utilization of nanoparticles and magnetic forces.

We aim to use the same principle to create a magnetic tamponade for RRD, utilizing a magnetic fluid bubble created from magnetic nanoparticles (MNPs) coated in biocompatible gel. MNPs can be specifically sized to elicit a desired superparamagnetic response and positioned against a retinal tear by using a magnetic helmet. The biocompatible gel bonds the MNPs and makes them fluid. Similar to silicon oil injection, this MNP fluid would be injected following air-fluid exchange and removal of subretinal fluid. It then has the potential to be removed through regular viscous extraction or kept within the eye given its biocompatibility. If this method were to replace the current postoperative positioning approach, it would have an immense benefit not only on quality of recovery in terms of convenience, but it would also increase the rate of successful reattachment. Currently, between 10–30% of cases require further intervention to correct failed reattachments [13,14]. Most failures occur early on in recovery, meaning a large portion will occur during a time when proper tamponade positioning plays such a large role in reattachment [15]. As posturing compliance determines tamponade position, this new approach could significantly decrease the current rate of failed reattachment. A helmet that positions

the tamponade without head posturing would therefore effectively eliminate failed reattachment due to compliance related failed tamponade placement. In this manuscript we explore simulations of several magnetic helmet designs to control intraocularly injected MNPs and create a magnetic tamponade for RRD repair. We then apply this data to construct a physical helmet for testing and successfully demonstrate capability of external excitation of MNPs using a magnetic helmet. It is our hope that the optimal helmet design could mimic the standard achieved with current practices while completely eliminating the requirement of head posturing postoperatively.

2. Methods

2.1. MNP force simulation tool

In order to analyze the effectiveness of the physical visor along with other theoretical designs, a proprietary simulation tool for calculating the magnetic force acting on MNPs within the vitreous humor was employed. Using the following formula 1:

$$\vec{F}_{mag} = \frac{4\pi a^3}{3}\frac{\mu_0 \chi}{\left(1+ \chi/_3\right)}\left[\frac{\partial \vec{H}}{\partial \vec{x}}\right]^T \vec{H} = \frac{2\pi a^3}{3}\frac{\mu_0 \chi}{\left(1+ \chi/_3\right)}\nabla\left(\left\|\vec{H}\right\|^2\right) \quad (1)$$

in which a is the radius of the particle, χ is the magnetic susceptibility of the particle, and H is the magnetic field at a given coordinate, the magnetic force acting on a single, spherical MNP was able to be calculated. By utilizing Finite Element Method Magnetics 4.2 (FEMM) and its included MATLAB function library, the magnetic field at a defined location on the plane that passes through the middle of the visor with respect to the z-axis was able to be simulated and programmatically extracted from the FEMM answer file (.ans) corresponding to the selected FEMM geometry file (.fem). Furthermore, using basic numerical methods, the derivatives of the x and y components of the magnetic field with respect to both axes were also able to be calculated. Using these results and derivative calculations combined with user inputted material and nanoparticle parameters, the simulation tool then calculated the magnetic forces acting on these MNP's and subsequently visualized the results.

The magnetic force acting on MNPs with a radius of 25 nm and a magnetic susceptibility of 20 in various magnetic fields created by different helmet designs was calculated at the 12 different locations representing the boundary of the globe (Figure 1).

2.2. Visor design

A metal visor was devised to better manipulate the strength and direction of the magnetic force acting on MNPs near the region of the eyes. The visor prototype for this study was composed entirely of galvanized steel, which was cut from a sheet of this metal, and was shaped in order fit around a human head (Figure 2a). The visor layered multiple strips of this steel and measured approximately 6 centimeters wide and 55 centimeters long. Keeping in mind that human heads vary in circumference, Velcro straps were attached to the ends of the metal strip to allow for easier adjustability and greater security on the patients' head. To additionally help the visor to stay in place, fastening straps were put around the perimeter of the visor in such a manner to create a helmet that

conformed to the top of the head. To realize the effects of including the visor for this study, a 2'' x 2'' x 1'' N45 magnet rated with a field of 500 mT was attached to the inner part of the visor.

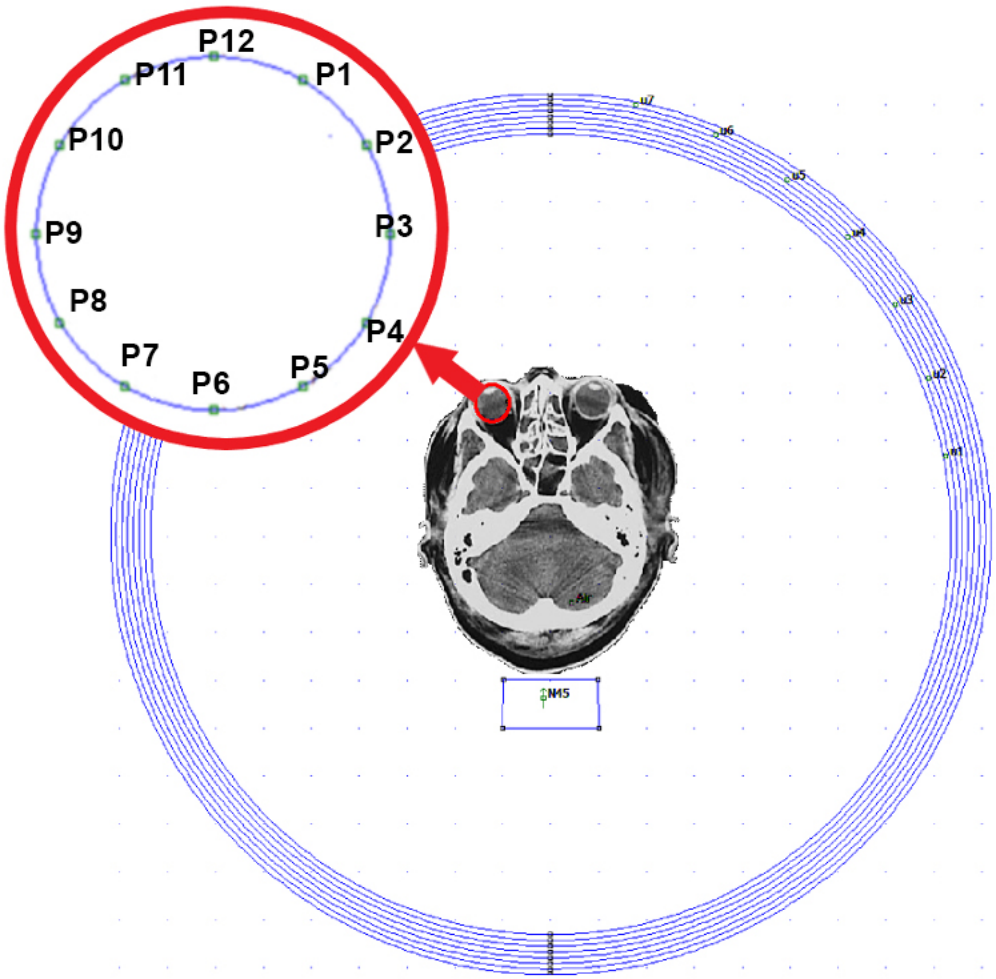

Figure 1. CT scan of a typical human head superimposed on top of the simulation field of a N45 magnet (Dimensions: 1'' x 2'' x 2'') positioned such that the North Pole is pointing towards the top of the page. Additionally, an enlarged image of the reference points P1 through P12 are included. These points are positioned around the radius of the right eye such that a point occurs every 30 degrees.

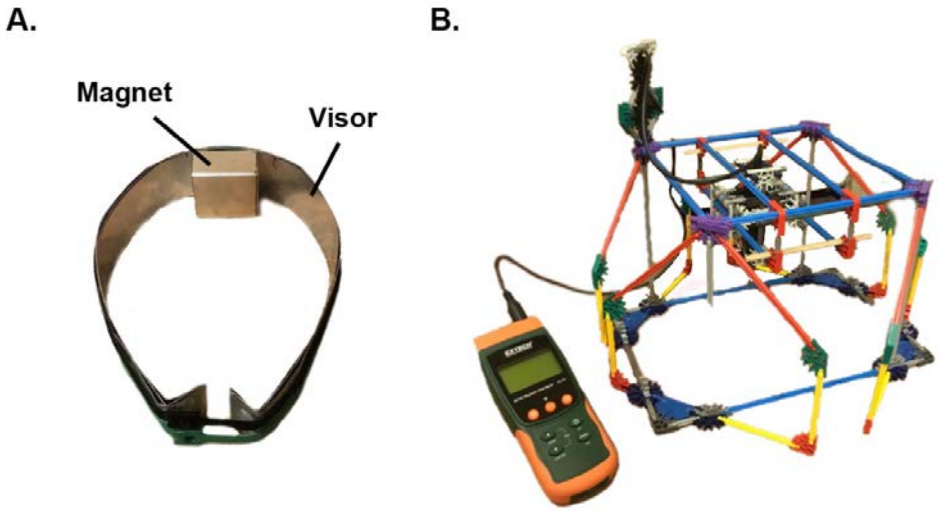

Figure 2. A. Physical visor composed of strips of galvanized steel with Velcro straps attached to the front of the visor to help maintain the visor's shape. Additionally, a N45 magnet (Dimensions: 1' x 2' x2') is fixed to the back of the visor. B. An Extech AD/DC Magnetic Field Meter (SDL900) and its corresponding probe configured within the adjustable plastic measuring apparatus that allows for steady measurements at a consistent distance from the bottom of the magnet.

Specifically, three helmet designs were simulated: a magnet at the back of the head alone, a back magnet with the addition of a metallic visor wrapping around to the front of the head ending in front of the eyes, and a back magnet and metallic visor with the addition of bends in front of the eyes (Figure 2a). Due to the lack of galvanized steel within FEMM's default material library, the material of the visor was defined as hot rolled low-carbon steel due to the similarity of the two materials. Additionally, local simulation correction factors were determined at each of the 12 points of interest in order to correct for the differences in the materials and other external factors.

2.3. Magnetic force measurement and simulation correction factors

An Extech AD/DC Magnetic Field Meter (SDL900) and a plastic adjustable measuring apparatus (Figure 2b) was used to measure the magnetic fieldlux with and without the visor at the 12 different points of interest representing the boundary of the globe. The plastic measuring apparatus was composed of a sparse framework and was positioned several inches away from the magnet on all sides and was used to hold the tip of the probe within the plane middle horizontal plane of the 2'' x 2'' x 1'' N45 magnet. The measurements taken for the setting without the visor were then compared to the corresponding simulated model of this singular N45 magnet in order to calculate the correction factor using formula 2: in order to derive local x and y simulation correction factors (Table 1) that were applied to all subsequent simulations. The resultant force at each point is the result of magnetic forces on the x and y directions, where each required a correction factor as follows:

$$CF_{i,x} = \frac{H_{i,x(measured)}}{H_{i,x\ (simulated)}};\ \ CF_{i,y} = \frac{H_{i,y(measured)}}{H_{i,y\ (simulated)}} \tag{2}$$

in which *CF* corresponds to the x and y correction factors for each of the 12 points of interest (*i*).

Using formula 1, the force formula with simulation corrections (formula 3) can be defined as:

$$\vec{F}_{i,mag} = \frac{4\pi a^3}{3}\frac{\mu_0 \chi}{\left(1+ \chi/_3\right)}\begin{bmatrix} CF_{i,x}\frac{\partial H_x}{\partial x} & CF_{i,x}\frac{\partial H_x}{\partial y} \\ CF_{i,y}\frac{\partial H_y}{\partial x} & CF_{i,y}\frac{\partial H_y}{\partial y}\end{bmatrix}^T \begin{bmatrix} CF_{i,x}H_x \\ CF_{i,y}H_y\end{bmatrix} \tag{3}$$

in which the local x and y correction factors are being applied to every value that is derived from the simulated magnetic field values.

3. Results

3.1. Simulation correction factor

Using formula 3, the simulated FEMM values were correlated with the recorded values of the Extech Field Meter. These values for the local correction values (Table 1) ranged from 0.220-0.305 for the x direction and 0.287-0.364 for the y direction.

Table 1. Local correction factors for the x and y components of the magnetic field for each of the 12 points of interest. The measured field values were measured using a Gauss metered for a physical representation of the "Magnet Only" setting. The simulated field values were derived from the "Magnet Only" FEMM simulation.

Correction Factor between Simulated and Physical Control Setting								
Points	Measured Field			Simulated Field			Local Correction Factor	
	x (mT)	y (mT)	Magnitude (mT)	x (mT)	y (mT)	Magnitude (mT)	x	y
P1	-0.78	2.66	2.772002886	-2.80392	8.87686	9.309168106	0.27818197	0.29965551
P2	-0.74	3.03	3.119054344	-2.6884	9.36208	9.740433075	0.27525666	0.32364603
P3	-0.75	3.28	3.364654514	-2.85829	9.91769	10.32135634	0.26239465	0.33072217
P4	-0.95	3.56	3.684575959	-3.11591	10.4499	10.90455433	0.30488685	0.34067312
P5	-1.01	3.92	4.048024209	-3.86618	10.7713	11.44413612	0.26123978	0.36393007
P6	-1.21	3.62	3.816870446	-4.56326	10.5097	11.45762348	0.26516131	0.3444437
P7	-1.29	3.26	3.505952082	-4.92443	9.91684	11.07220513	0.26195925	0.32873375
P8	-1.31	3	3.273545479	-4.98637	9.2756	10.53093733	0.26271616	0.32342921
P9	-1.2	2.72	2.972944668	-4.7709	8.72688	9.945849453	0.25152487	0.31168069
P10	-1.03	2.42	2.630076045	-4.2571	8.43947	9.452383524	0.24194874	0.28674786
P11	-0.85	2.43	2.57437371	-3.72808	8.4494	9.235309461	0.2279994	0.28759439
P12	-0.7	2.56	2.653978146	-3.18681	8.56667	9.140218425	0.21965539	0.29883257

3.2. Validation of the simulation correction factors using the physical prototype

In order to validate the local correction factors calculated, additional physical and simulated field measurements were collected for the physical visor design representing the "Helmet with Bends" setting and its corresponding FEMM file. As with the previous simulations, 12 points representing the

relative boundary of the eye were used as points for measuring the physical and simulated helmet (Table 2).

Initial physical measurements proved to be smaller than those simulated at each corresponding point. This decrease in field strength going from the simulations to the physical prototype is likely caused by the obfuscation of the magnetic flux due to the non-ideal surface interfaces between the magnet and the layers used to create the visor in addition to other slight material imperfections found within the N45 magnet and galvanized steel. However, even with this slight decrease between the measured the simulated fields, the overall percent error was relatively low with an average of 5.48% and standard deviation of 3.32% (Table 2).

Table 2. The measured and corrected simulated field for each of the 12 points of interest for the "Helmet with Bends" setting. The measured field values were measured from a physical magnet and metallic visor representing the "Helmet with Bends" setting while the simulated field values were derived from the "Helmet with Bends" FEMM simulation. These simulated field values were then corrected for using the corresponding local correction factor.

Physical Validation for Helmet w/Bends Setting							
Points	Measured Field (Helmet w/ Bends)			Corrected Simulated Field (Helmet w/ Bends)			% Error
	x (mT)	y (mT)	Magnitude (mT)	x (mT)	y (mT)	Magnitude (mT)	
P1	-0.46	2.84	2.877012339	-0.546107378	2.665456727	2.720825763	5.43%
P2	-0.56	3.17	3.219083721	-0.582434831	3.273453015	3.324864655	3.29%
P3	-0.65	3.39	3.451753178	-0.682079145	3.548384352	3.613345191	4.68%
P4	-0.87	3.56	3.664764658	-1.001928329	3.837478253	3.966118975	8.22%
P5	-1.08	3.8	3.95049364	-1.130611793	4.104148617	4.2570317	7.76%
P6	-1.41	3.51	3.782618141	-1.449589153	3.759740811	4.029511097	6.53%
P7	-1.58	3.11	3.488337713	-1.602708618	3.326292448	3.692275229	5.85%
P8	-1.89	2.83	3.403086834	-1.603511753	2.940825391	3.349582649	1.57%
P9	-1.46	2.52	2.912387337	-1.39297491	2.51458684	2.874634946	1.30%
P10	-1.34	2.41	2.757480734	-1.125110051	2.125352232	2.404785799	12.79%
P11	-0.96	2.23	2.427859139	-0.807243273	2.119337669	2.267869894	6.59%
P12	-0.59	2.31	2.384156035	-0.543717385	2.362722692	2.424476668	1.69%

3.3. Theoretical analysis for helmet designs

The three design settings represented in Figure 3 were simulated (Table 3). These recorded values represent forces placed on both the x and y plane and their resulting total magnitude of force. Looking at the magnetic force data displayed in Table 3 for the "Magnet Only" setting, the total forces range from 9.76E^-21-3.04E^-20 N on each nanoparticle. As expected, the magnetic force generated is primarily directed in the negative y direction toward the magnet. For this geometry, all 12 points had forces placed in the medial direction.

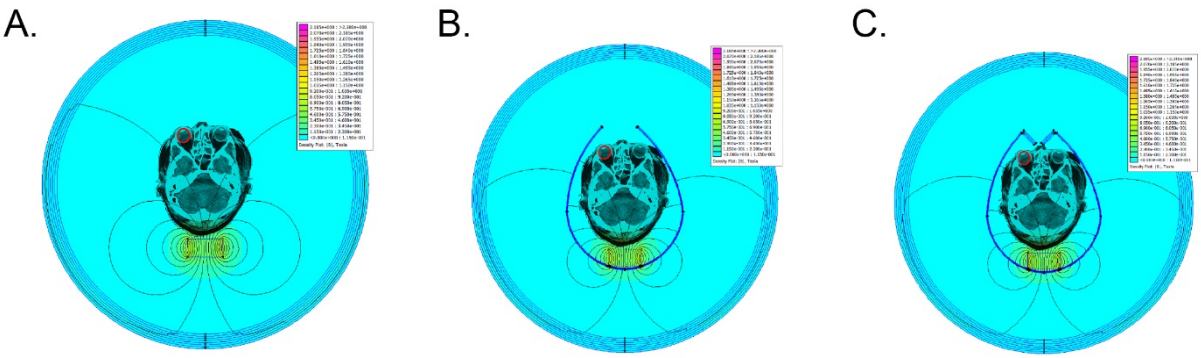

Figure 3. Simulation of different magnet and helmet configurations. CT scan of a typical human head superimposed on top of the simulated field of a N45 magnet (Dimensions: 1'' x 2'' x 2'') for representation of the construct. A. "Magnet Only" simulation setting which only compromise a N45 magnet. B. The "Helmet Default" simulation setting and C. "Helmet with Bends" simulation setting. The circle that encompasses points P1-P12 is shown in red identifying the eye of interest (right eye).

Table 3. Values for the components and magnitude of the magnetic forces applied on magnetic nanoparticles (r = 25 nm, χ = 20) located at each of the 12 points of interest for each of the simulation settings.

Magnetic Force Data for Different Settings									
Points	Magnet-Only			Default-Helmet			Helmet w/ Bends		
	x (N)	y (N)	Magnitude (N)	x (N)	y (N)	Magnitude (N)	x (N)	y (N)	Magnitude (N)
P1	1.35E-21	-1.24E-20	1.25E-20	2.49E-21	-1.69E-20	1.71E-20	2.02E-20	-1.61E-20	2.58E-20
P2	1.98E-21	-1.64E-20	1.65E-20	8.43E-22	-2.02E-20	2.02E-20	2.85E-20	-1.45E-20	3.20E-20
P3	3.18E-21	-1.88E-20	1.91E-20	3.30E-21	-2.39E-20	2.41E-20	2.23E-20	-2.36E-20	3.25E-20
P4	2.06E-21	-2.37E-20	2.37E-20	4.52E-21	-3.48E-20	3.51E-20	1.55E-20	-3.22E-20	3.57E-20
P5	7.20E-21	-2.96E-20	3.04E-20	7.21E-21	-4.41E-20	4.47E-20	1.77E-20	-3.37E-20	3.81E-20
P6	1.16E-20	-2.37E-20	2.63E-20	4.95E-21	-4.14E-20	4.17E-20	1.04E-20	-3.80E-20	3.94E-20
P7	9.49E-21	-1.89E-20	2.11E-20	3.24E-21	-3.72E-20	3.74E-20	1.11E-20	-3.58E-20	3.75E-20
P8	8.16E-21	-1.62E-20	1.81E-20	1.05E-21	-2.83E-20	2.84E-20	6.51E-21	-3.32E-20	3.38E-20
P9	5.90E-21	-1.34E-20	1.46E-20	1.04E-22	-2.34E-20	2.34E-20	2.98E-21	-2.70E-20	2.71E-20
P10	3.82E-21	-1.03E-20	1.10E-20	2.69E-21	-1.48E-20	1.51E-20	3.22E-21	-1.83E-20	1.86E-20
P11	4.19E-21	-8.81E-21	9.76E-21	5.52E-22	-1.63E-20	1.63E-20	8.47E-21	-1.76E-20	1.96E-20
P12	1.97E-21	-1.14E-20	1.16E-20	4.14E-21	-1.52E-20	1.58E-20	1.47E-20	-2.04E-20	2.51E-20

For the "Default Helmet" setting, a visor was added to the back magnet. With the addition of the visor, a significant increase in total force was created, ranging from 1.51-4.47E^-20 N. Again, the y component of the magnetic force vectors simulated is many times larger than the x component. For this design, however, the addition of the visor resulted in a larger x component of force that had more influence on the resulting magnetic force vector.

For the "Helmet with Bends" setting, a bend was placed on both sides of the front portions of the visor. The total force magnitudes for this simulation ranged from 1.86-3.94E10^-20 N, showing

an increase for nearly all points compared to the other designs, barring P5-P6 of the "Default Helmet" design outperforming the "Helmet with Bends" design.

3.4. Comparison of helmet designs

From this data and its subsequent visualizations (Figures 4 and 5), several important trends were noticed in regard to all three simulations. As expected with the "Magnet Only" simulation, there was an increase in the total magnitude of forced placed on the various positions, most notably, there was an increase from the anterior to the posterior of the eye with a 1.273-fold increase from P12 to P6. This is even more so for the "Default Helmet" geometry with the addition of a visor, having a 1.647-fold increase from P12 to P6. With the addition of the bends in the "Helmet with Bends" design, there is only a 0.568-fold increase in total magnitude of force from front to back between P12 and P6. This discrepancy, however, is due to larger x-coordinate forces being placed on the front positions contributing to larger total force.

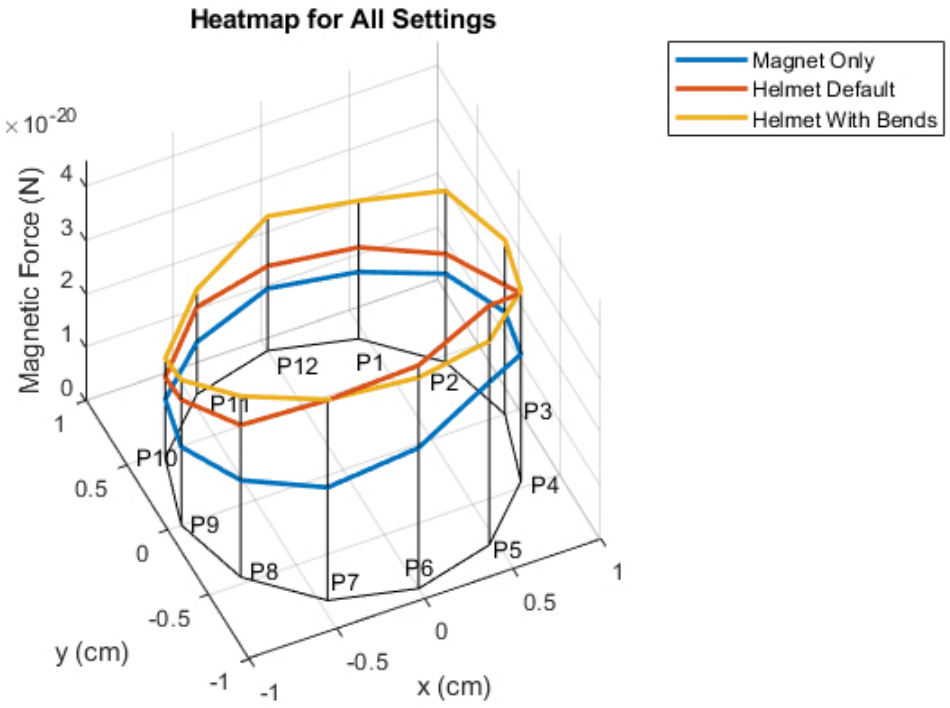

Figure 4. Magnitude of magnetic forces acting on a magnetic nanoparticle (r = 25 nm, χ = 20) located at each of the 12 points of interest for each of the simulation settings. The front and back of the eye have additionally been labeled for reference.

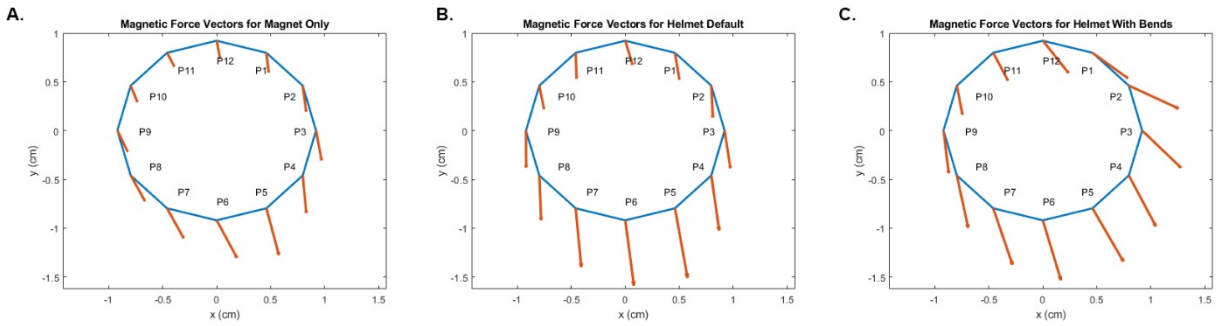

Figure 5. **A.** Direction of scaled magnetic forces vectors acting on a magnetic nanoparticle (r = 25 nm, $\chi = 20$) located= at each of the 12 points of interest for each of the "Magnet Only" simulation setting. The front and back of the eye have additionally been labeled for reference. **B.** Direction of scaled magnetic forces vectors acting on a magnetic nanoparticle (r = 25 nm, $\chi = 20$) located= at each of the 12 points of interest for each of the "Helmet Default" simulation setting. The front and back of the eye have additionally been labeled for reference. **C.** Direction of scaled magnetic forces vectors acting on a magnetic nanoparticle (r = 25 nm, $\chi = 20$) located= at each of the 12 points of interest for each of the "Helmet with Bends" simulation setting. The front and back of the eye have additionally been labeled for reference.

For the y component of force for each design, the increase from P12 to P6 was 1.072-fold, 1.724-fold, and 0.862-fold respectively for the three aforementioned settings. Notably, while the increase from P12 to P6 was proportionally the smallest for the "Helmet with Bends" setting, the average magnitude for the y component of force between these two points was the largest for the "Helmet with Bends" setting (2.92E^-20) when compared to the "Magnet Only" (2.83E^-20) and "Default Helmet" (1.75E^-20) settings. Furthermore, including the metallic visor with the "Default Helmet" and "Helmet with Bends" settings resulted in the magnitude of the y component of force increasing for every point when compared to the "Magnet Only" setting barring P2 from the "Helmet with Bends" setting. When these two visor settings are compared directly, the "Default Helmet" outperforms the "Helmet with Bends" setting for 7 of the 12 points of interest (P1-P7). This would suggest that the "Default Helmet" setting would be best suited for applications where force would need to be applied directly to the posterior of the eye.

In respect to the x component of force, the direction was the same for all points in each simulation; however, the magnitude varied greatly based on design. Most notably, 7 of the 12 points for the "Default Helmet" setting (P2; P6-P11) saw a decrease in the x component of force in comparison to the "Magnet Only" setting. Conversely, only 4 of the 12 points for the "Helmet with Bends" setting (P6; P9-P10) followed the same trend. However, the x component of force for the "Helmet with Bends" setting increased at all points when compared to the "Default Helmet" setting. This would suggest that the "Helmet with Bends" design setting would be best utilized in applications where significant force needs to be additionally applied to the sides of the eye.

4. Discussion

Within the last two decades, there has been a surge in research focusing on MNPs and their use in many areas of science and technology [16]. Within the field of medicine, MNPs have shown potential to revolutionize modern therapeutic approaches. These materials offer such an extensive range of utility mainly due their ability to be coupled with drugs and other materials. For the purpose of targeted therapy, however, it is not enough to have biocompatible drug-eluting MNP carriers. The placement of an external magnetic field for the purpose of precise manipulation and positioning is also needed [17]. With magnetic manipulation MNPs promise an even wider advantage.

The application of an external magnet to control MNPs within biological tissue for the purpose of targeted therapy has been used in several areas. One of the critical complications with current chemotherapy technique is the inability to attack only tumor cells without killing normal tissue. One study successfully demonstrated that magnetic manipulation of MNPs might be the solution to this problem [18]. In this study, doxorubicin bound nano-carriers were targeted toward tumor cells in rats using an external magnet. Compared to the control, the resulting tumor size was decreased with reduced toxicity for normal tissue. In the effort to deliver drug therapy for inner ear diseases, MNP control has been tested on guinea pigs to pull drug-coated MNPs through the round window membrane into the middle ear by placement of a magnet on the contralateral side [19].

There have been a select few studies that have focused on magnetic manipulation within the eye. In a study with rats, a magnetic push mechanism was used to inject MNPs toward the retina [17]. Still, there has yet to be a study that has demonstrated the utility of a helmet designed to manipulate MNPs for the purpose of RRD repair.

In this study, we have demonstrated the utility of including a magnetic system within our helmet designs to create a magnetic tamponade for RRD. Other studies have shown improved therapy by concentrating MNPs into a desired location using an external magnet [19]. Similarly, we sought to concentrate MNPs against the retina using similar techniques. Beginning with virtual simulations, we have shown that a visor is needed in addition to a back magnet to generate a stronger force than can be achieved with a back magnet alone. After gathering data from the theoretical simulations, we designed a physical prototype helmet to observe how a design would translate from virtual simulation to reality. With our experimentation, we demonstrated that the same trends we observed virtually translated successfully to a physical helmet design with minimal error. We have shown that this physical design has utility to pull MNPs into the back of the eye. In this manuscript, we calculated the magnetic force placed on one MNP. In real world application, the surgeon can determine the amount of liquid to cover the entire retina and generate enough force to stabilize it in place using calculation. A set volume of fluid contains a precise number of MNPs and therefore the amount of force per area of coverage can be calculated. Additionally, the surgeon can adjust the strength and positioning of the magnet to control force and direction to keep the retina at the desired position. Though our experimentation has not actually tested MNPs within the vitreous body of the eye, we believe MNPs when injected will be directed by the gradients described in this manuscript by controlling the distance and strength of the magnet as well as the density of the fluid to determine the amount of MNPs required. To prevent MNP penetration into the cells of the retina, the MNPs will be meshed together with a biocompatible polymer that prevents penetration or absorption. This polymer will surround the MNPs and therefore the MNPs will not directly come into contact with the cells. This also avoids the potential for creation of toxic compounds.

It is our hope to design a better method for recovery from RRD surgery. Our goal was to design a helmet that could magnetically control intraocular MNPs to create a magnetic tamponade and thereby eliminate the need for postoperative head positioning. As of now, we have only experimented with a physical prototype that includes a back magnet and a visor with bends angled in front of the eyes. This design shows promising capability to apply force to the retina. This may serve as an advantage for nasal RRD tears as its forces are posteromedially directed. Though we did not design a physical helmet for the visor without bends designs, virtual simulations show that this physical design would have an advantage for temporal RRD tears, as its forces are more posterolaterally directed.

As we have shown through virtual and physical simulation that the addition of a visor generates a greater magnitude of force compared to a back magnet alone, future designs are needed to take advantage of this. Future designs might include the addition of metal coils toward the front to further extend the magnetic flux through the visor. Experimenting with different materials could also improve the field strength and optimize directionality of the forces. Overall, the current designs in this manuscript are a strong starting point for demonstrating our novel approach for RRD recovery as the results show promise for MNP manipulation.

Acknowledgments

The authors would like to thank for the help of Dr. Yi Yi in the project.

Financial Support: Multidisciplinary University Research Initiative award Indiana University, Glick Eye Institute Departmental Research Support and Research to Prevent Blindness, Indiana University.

Conflict of interest

AI and AH are patent inventors.

Reference

1. C. Wong, W. Wong, I. Yeo, B. Loh, E. Wong, D. Wong, et al., Trends And Factors Related To Outcomes For Primary Rhegmatogenous Retinal Detachment Surgery In A Large Asian Tertiary Eye Center, *Retina.*, **34** (2014), 684–692.
2. J. Hwang, Regional practice patterns for retinal detachment repair in the United States, *Am. J. Ophthalmol.*, **153** (2012), 1125–1128.
3. F. Kuhn, B. Aylward, Rhegmatogenous Retinal Detachment: A Reappraisal of Its Pathophysiology and Treatment, *Ophthalmic Res.*, **51** (2014), 15–31.
4. M. Johnson, Postoperative Positioning Following RD Surgery, *Retinal Physician*, **10** (2013), 25–29.
5. M. Kita, A. Negi, S. Kawano, Y. Honda, Photothermal cryogenic, and diathermic effects on retinal adhesive force in vivo, *Retina*., **11** (1991), 441–444.
6. O. Kwon, S. Kim, Changes in adhesive force between the retina and the retinal pigment epithelium by laser photocoagulation in rabbits, *Yonsei Med. J*., **36** (1995), 243–250.
7. L. Poliner, P. Tornambe, Failed retinal detachment repair after intravitreal air injection, *Arch. Ophthalmol.*, **107** (1989), 487–488.

8. Y. Yoon, M. Marmor, Rapid enhancement of retinal adhesion by laser photocoagulation, *Ophthalmology.*, **95** (1988), 1385–1388.
9. R. Ajlan, J. Isenberg, G. Cordahi, R. Duval, S. Olivier, F. Rezende, Primary rhegmatogenous retinal detachment with inferior retinal breaks postoperative prone positioning results: 1 day versus 7 days, *Int. J. Retin. Vitr.*, **3** (2017), 1–6.
10. G. Hilton, T. Das, A. Majji, S. Jalali, Pneumatic retinopexy-principles and practice, *Indian J. Ophthalmol*., **4** (1996), 131–143.
11. S. Stewart, W. Chan, Pneumatic retinopexy: patient selection and specific factors. *Clin. Ophthalmol.*, **12** (2018), 493–502.
12. Y. Seno, Y. Shimada, T. Mizuguchi, A. Tanikawa, M. Horiguchi, Compliance with the face-down positioning after vitrectomy and gas tamponade for rhegmatogenous retinal detachments, *Retina*., **35** (2015), 1436–1440.
13. D. Steel, Retinal Detachment, *BMJ Clin. Evid.*, (2014), 0710.
14. R. Adelman, A. Parnes, D. Ducournau, European Vitreo-Retinal Society (EVRS) Retinal Detachment Study Group, Strategy for the management of uncomplicated retinal detachments: The European Vitreo-Retinal Society Retinal Detachment study report 1, *Ophthalmology*., **120** (2013), 1804–1808.
15. M. Choudhary, M. Choudhary, M. Saeed, A. Ali, Removal of silicone oil: Prognostic factors and incidence of retinal redetachment, *Retina*., **32** (2012), 2034–2038.
16. K. Wu, D. Su, J. Liu, R. Saha, J. Wang, Magnetic nanoparticles in nanomedicine: a review of recent advances, *Nanotech.*, **30** (2019), 502003.
17. B. Shapiro, S. Kulkarni, A. Nacev, A. Sarwar, D. Preciado, D. Depireux, Shaping Magnetic Fields to Direct Therapy to Ears and Eyes, *Ann. Rev. Biomed. Eng.*, **16** (2014), 455–481.
18. P. Liang, Y. Chen, C. Chiang, L. Mo, S. Wei, W. Hsieh, et al., Doxorubicin-modified magnetic nanoparticles as a drug delivery system for magnetic resonance imaging-monitoring magnet-enhancing tumor chemotherapy, *Int. J. Nanomed.*, **11** (2016), 2021–2037.
19. R. Kopke, R. Wassel, F. Mondalek, B. Grady, K. Chen, J. Liu, et al., Magnetic nanoparticles: Inner ear targeted molecule delivery and middle ear implant, *Audiol Neurotol.*, **11** (2006), 123–133.